Background-Force Compensation in Dynamic Atomic Force Microscopy

Riccardo Borgani,[1,*] Per-Anders Thorén,[1] Daniel Forchheimer,[1] Illia Dobryden,[2] Si Mohamed Sah,[1] Per Martin Claesson,[2] and David B. Haviland[1]

[1]*Nanostructure Physics, KTH Royal Institute of Technology, Stockholm SE-106 91, Sweden*
[2]*Surface and Corrosion Science, KTH Royal Institute of Technology, Stockholm SE-100 44, Sweden*
(Received 16 December 2016; revised manuscript received 17 March 2017; published 13 June 2017)

Background forces are linear long-range interactions of the cantilever body with its surroundings that must be compensated for in order to reveal tip-surface force, the quantity of interest for determining material properties in atomic force microscopy. We provide a mathematical derivation of a method to compensate for background forces, apply it to experimental data, and discuss how to include background forces in simulation. Our method, based on linear-response theory in the frequency domain, provides a general way of measuring and compensating for any background force and it can be readily applied to different force reconstruction methods in dynamic AFM.

DOI: 10.1103/PhysRevApplied.7.064018

I. INTRODUCTION

Accurate and reproducible measurement of material properties at the nanoscale is the main goal of dynamic atomic force microscopy (AFM). Extraction of material properties from the measurable quantities in dynamic AFM requires a deep understanding of both the tip-surface interaction and the dynamics of the AFM cantilever when it is close to the sample surface. We propose a method that uses Fourier analysis to measure and compensate for background forces, which are long range and not local to the AFM tip. These interactions produce artifacts in the measurement of tip-surface force, leading to overestimation of its attractive and dissipative components.

Background forces are observed when measuring the quality factor of a cantilever resonance which decreases when the tip-sample distance becomes comparable to the cantilever width, dropping as much as 30% at the scanning position (Fig. 1). This phenomenon has been attributed to an additional squeeze-film damping force [1–3], arising when the fluid surrounding the cantilever is squeezed between the cantilever body and the sample surface. We also observe a slight decrease in the resonance frequency f_0, due to increased hydrodynamic load.

Other long-range forces appearing at tip-sample distances of a few micrometers have been attributed to electrostatic contributions [4]. We have also observed in different commercial AFM systems, a dependence of the cantilever's acoustic excitation on the z extension of the piezoelectric scanner, resulting in a change of the drive force which can be mistaken as a long-range interaction. The coupling between the cantilever and the acoustic actuator could in principle also be affected by the increased hydrodynamic load, causing the effective drive power to change as a function of the tip-sample distance.

Whatever their origin, be it hydrodynamic, electrostatic, or AFM design, these effects influence force reconstruction in dynamic AFM. Previous attempts at compensating for them have used an effective resonance frequency and quality factor for the cantilever [5–7], but a general and accurate description is still lacking. Here, we describe how to compensate for these effects by treating them as

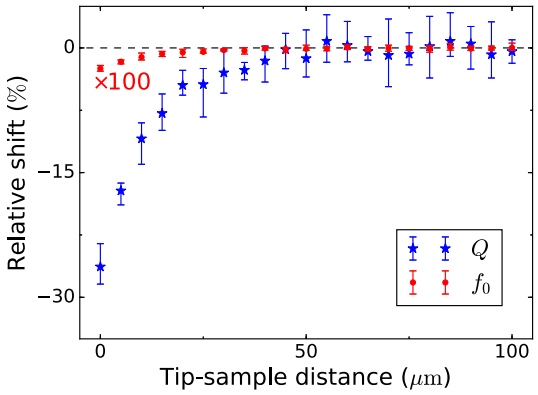

FIG. 1. Relative change in quality factor Q and resonance frequency f_0 as a function of tip-sample distance over a homogeneous polydimethylsiloxane surface. The values are obtained by fitting the thermal-noise power-spectral density, and plotted as the shift relative to a tip-sample distance of 1 mm. The fitted Q drops by as much as 30%, whereas the decrease in f_0 is 3 orders of magnitude smaller (plotted values of f_0 are multiplied by 100). The cantilever is a MikroMasch HQ:NSC15/AlBS.

*borgani@kth.se

background forces, assuming that they have the following properties: they are linear as shown by a lack of intermodulation distortion [8]; they act over a long range, comparable to the cantilever width; and they do not depend on the xy tip position over the sample surface, as they originate from the cantilever body rather than being local to the tip.

We can easily compensate for any such background force to reveal the true tip-surface interaction, using linear-response theory in the frequency domain. Because of its generality and ease of implementation, we expect our method to be readily applied to a variety of force reconstruction methods essential for AFM researchers.

II. GENERIC LINEAR MODEL

When an AFM cantilever is far away from the sample surface, its fundamental flexural mode is well modeled as a linear system. The frequency-dependent linear-response function $\hat{\chi}(\omega)$ relates the frequency components of any force $\hat{F}(\omega)$ to the resulting frequency components of the cantilever deflection $\hat{d}(\omega)$:

$$\hat{d}(\omega) = \hat{\chi}(\omega)\hat{F}(\omega). \tag{1}$$

In our notation $\hat{d}(\omega)$ denotes a complex valued function of the real variable ω, the frequency. In particular, $\hat{d}(\omega)$ is the Fourier transform of $d(t)$. In the following, we will drop the explicit ω dependence for the sake of compact notation.

When the frequency components of $\hat{d}$ are concentrated around the cantilever resonance frequency, $\hat{\chi}$ can be well modeled as a dampened simple harmonic oscillator:

$$\hat{\chi}^{-1} = k\left(1 - \frac{\omega^2}{\omega_0^2} + i\frac{\omega}{Q\omega_0}\right). \tag{2}$$

The parameters k, ω_0, and Q are the mode stiffness, resonance frequency, and quality factor, respectively. These parameters, together with the optical-lever responsivity, can be obtained by a noninvasive calibration procedure traceable to the measurement of the thermal fluctuations of the cantilever deflection when it is far from the surface [9,10].

The drive force with multiple frequency components $\hat{F}_D$ is applied to the cantilever by means of a shaker piezoelectric actuator in the case of acoustic excitation, or a pulsed laser beam in the case of photothermal excitation. Regardless of the means of excitation, the drive force is determined by measuring the cantilever motion far away from the surface (larger than 100 μm) at what we call the "free" position [Fig. 2(a)]. Thus, we extract the driving force from a measurement of the cantilever free motion $\hat{d}_{\text{free}}$ and the calibrated linear-response function $\hat{\chi}$

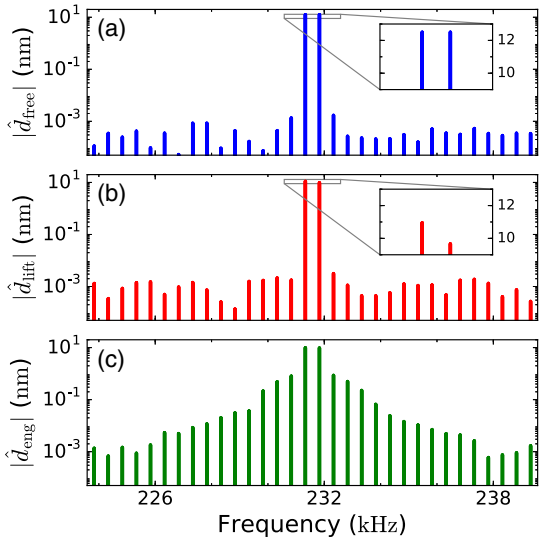

FIG. 2. Discrete frequency spectra of cantilever motion measured near resonance using a two-tone drive. Phase is also measured at each frequency but only amplitude is shown. (a) At the free position far away from the sample surface. (b) At the lift position closer to the surface. (c) At the engaged position on a polystyrene surface. In (a) and (b) linear forces act on the cantilever and only noise is measured at the undriven frequencies. In (c) the nonlinear tip-surface force gives rise to intermodulation with strong response at undriven frequencies.

$$\hat{F}_D = \hat{\chi}^{-1}\hat{d}_{\text{free}}. \tag{3}$$

As the AFM probe approaches the sample surface, background forces begin to affect the cantilever body when its separation from the surface becomes comparable to its width, as shown in Fig. 1. Background forces change the cantilever motion [compare insets of Figs. 2(a) and 2(b)], but they are clearly linear, as seen from the lack of intermodulation [8] in the spectrum of Fig. 2(b).

When the AFM tip starts interacting with the surface at what we call the "engaged" position [Fig. 2(c)], the measured motion is affected by all the forces at play

$$\hat{d}_{\text{eng}} = \hat{\chi}(\hat{F}_D + \hat{F}_{\text{BG}} + \hat{F}_{\text{TS}}), \tag{4}$$

where $\hat{F}_{\text{TS}}$ is the nonlinear tip-surface force, carrying all the information about the material properties, and $\hat{F}_{\text{BG}}$ are the background forces. We can use Eq. (3) to account for the drive force, but in order to solve for the tip-surface force we must eliminate the background forces.

Note that, while the components of the drive force $\hat{F}_D$ can be treated as constant, the components of the background forces $\hat{F}_{\text{BG}}$ depend on the motion $\hat{d}$ which changes from pixel to pixel. For example, a squeeze-film damping force will depend on the velocity of the cantilever.

Motivated by experimental observation (the lack of intermodulation distortion), we treat the problem of a general linear background force without regard to its particular

origin, by expressing it in terms of a linear-response function $\hat{\chi}_{\mathrm{BG}}$

$$\hat{F}_{\mathrm{BG}} = \hat{\chi}_{\mathrm{BG}}^{-1}\hat{d}. \tag{5}$$

Equation (5) allows for the calculation of $\hat{F}_{\mathrm{BG}}$ for any motion $\hat{d}$. Our treatment assumes that there exists a linear differential equation of the cantilever deflection which describes the background forces. This equation can in principle be very complicated, e.g., involve fractional derivatives and have many parameters, but we assume that it does not change as the probe scans over the sample, consistent with the idea that the background forces act on the body of the cantilever.

Lifting the probe slightly away from the surface, we find that the short-ranged $\hat{F}_{\mathrm{TS}}$ goes to zero with an abrupt drop in intermodulation, while the long-ranged $\hat{F}_{\mathrm{BG}}$ is barely affected. We define the "lift" position as the closest distance for which the forces acting on the cantilever are linear (see Sec. III).

At the lift position [Fig. 2(b)], the total force is given by the drive force $\hat{F}_D$ and the linear background forces $\hat{F}_{\mathrm{BG}}$ only. The lift motion is therefore

$$\hat{d}_{\mathrm{lift}} = \hat{\chi}\hat{F}_D + \hat{\chi}\hat{F}_{\mathrm{BG}}. \tag{6}$$

Solving for $\hat{F}_{\mathrm{BG}}$ gives

$$\hat{F}_{\mathrm{BG}} = \hat{\chi}^{-1}\hat{d}_{\mathrm{lift}} - \hat{F}_D. \tag{7}$$

Combining Eqs. (3), (5), and (7), we determine $\hat{\chi}_{\mathrm{BG}}$ from the measured $\hat{d}_{\mathrm{free}}$ and $\hat{d}_{\mathrm{lift}}$

$$\hat{\chi}_{\mathrm{BG}}^{-1} = \hat{\chi}^{-1}\frac{\hat{d}_{\mathrm{lift}} - \hat{d}_{\mathrm{free}}}{\hat{d}_{\mathrm{lift}}}. \tag{8}$$

Going back to the engaged position, we can now compensate for the background forces in Eq. (4) using $\hat{\chi}_{\mathrm{BG}}$ from Eq. (8). Thus, we obtain the tip-surface force

$$\hat{F}_{\mathrm{TS}} = \hat{\chi}^{-1}\hat{d}_{\mathrm{eng}} - \hat{F}_D - \hat{\chi}_{\mathrm{BG}}^{-1}\hat{d}_{\mathrm{eng}}. \tag{9}$$

Equation (9) allows for the compensation of the background forces, and thus the calculation of the tip-surface force at every pixel of an AFM image, provided the knowledge of $\hat{F}_D$ and of $\hat{\chi}_{\mathrm{BG}}$, both being constant during the AFM scan.

III. DEFINING THE LIFT POSITION

To accurately determine the linear-response function of the background forces $\hat{\chi}_{\mathrm{BG}}$, we need to measure the cantilever motion $\hat{d}_{\mathrm{lift}}$ as close to the surface as possible without tip-surface interaction. We use the notion that the tip-surface force is strongly nonlinear, while the background forces are linear, as evidenced by the measurements of Figs. 2 and 3.

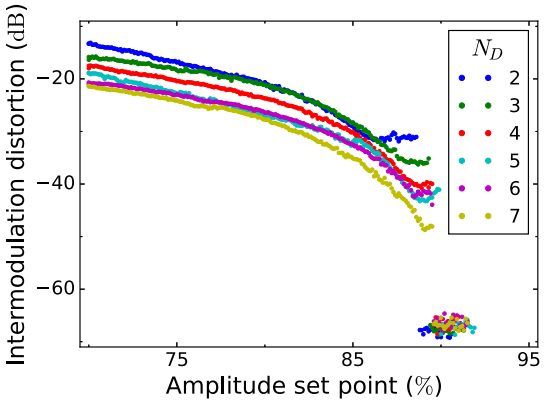

FIG. 3. Intermodulation distortion (IMD) for a different number of drive tones N_D is measured as a function of the AFM feedback amplitude set point. As the AFM probe moves away from the surface (increasing the set point), IMD gradually decreases until the probe suddenly breaks free from the tip-surface interaction F_{TS} and a sharp drop in IMD is observed. The lift motion is measured at this drop. For all data shown, the total free amplitude is 50 nm.

We apply a multifrequency drive with a number of discrete components N_D at the set of frequencies $\{\omega_{Dk}\}$ with $N_D \geq 2$, i.e., $\hat{F}_D(\omega)$ is nonzero for $\omega \in \{\omega_{Dk}\}$. When the linear forces $\hat{F}_D$ and $\hat{F}_{\mathrm{BG}}$ act on the cantilever, the response $\hat{d}(\omega)$ will be nonzero only at $\omega \in \{\omega_{Dk}\}$ [see Figs. 2(a) and 2(b)]. On the other hand, when the cantilever is experiencing the nonlinear $\hat{F}_{\mathrm{TS}}$, response will arise at intermodulation product frequencies ω_{IMP} given by integer linear combinations of the drive frequencies:

$$\omega_{\mathrm{IMP}} = \sum_{k=1}^{N_D} n_k\omega_{Dk}, \qquad n_k \in \mathbb{Z}, \tag{10}$$

where n_k is an integer [see Fig. 2(c)].

We introduce the intermodulation distortion IMD, as the ratio of the power at undriven frequencies to the power at driven frequencies:

$$\mathrm{IMD} = \frac{\sum_{\omega_{\mathrm{IMP}}\notin\{\omega_{Dk}\}}|\hat{d}(\omega_{\mathrm{IMP}})|^2}{\sum_{\omega_{\mathrm{IMP}}\in\{\omega_{Dk}\}}|\hat{d}(\omega_{\mathrm{IMP}})|^2}. \tag{11}$$

In principle, we want to measure $\hat{d}_{\mathrm{lift}}$ at the minimum distance from the surface such that IMD = 0. In practice, however, we will always measure some nonzero noise power. We therefore choose a threshold (typically 3 dB) and measure $\hat{d}_{\mathrm{lift}}$ at the minimum distance from the surface such that $\mathrm{IMD}_{\mathrm{lift}} < \mathrm{IMD}_{\mathrm{free}} + \mathrm{threshold}$.

Figure 3 shows the intermodulation distortion as a function of amplitude set point measured for drive schemes with a different number of drive tones N_D. As the AFM

feedback set point increases, a characteristic behavior is visible showing a gradual decrease of IMD with an increasing set point, due to the decrease of the nonlinear tip-surface interaction $\hat{F}_{\mathrm{TS}}$. When the set point reaches a value of about 90%, a sharp drop in IMD is observed, indicating a transition from an overall nonlinear force to an overall linear force. This sharp transition allows for unambiguous measurement of $\hat{d}_{\mathrm{lift}}$, from which we calculate the linear-response function of the background forces $\hat{\chi}_{\mathrm{BG}}$.

IV. EXTRAPOLATION TO UNDRIVEN FREQUENCIES

As discussed in Sec. III, $\hat{d}_{\mathrm{lift}}$ and $\hat{d}_{\mathrm{free}}$ will be nonzero only at the drive frequencies. Calculating the linear-response function of the background forces from Eq. (8) will, therefore, yield $\hat{\chi}_{\mathrm{BG}}(\omega)$ only at the drive frequencies $\omega \in \{\omega_{Dk}\}$. On the other hand, to apply the compensation to the measured data with Eq. (9) we require the knowledge of $\hat{\chi}_{\mathrm{BG}}(\omega)$ at all the frequencies in the spectrum of engaged motion $\hat{d}_{\mathrm{eng}}$.

To overcome this issue we use the notion of narrow-band measurement on a resonant system. Because of the high Q resonance in the cantilever linear-response function, the motion will be concentrated at frequencies close to the resonance frequency ω_0, within a narrow band Ω

$$\Omega \approx N_{\mathrm{IMP}} \frac{\omega_0}{Q} \ll \omega_0, \tag{12}$$

where N_{IMP} is the number of measured frequencies (typically 32) and ω_0/Q is typically chosen as the measurement bandwidth. We perform a polynomial expansion of the complex function $\hat{\chi}_{\mathrm{BG}}(\omega)$ in this narrow band:

$$\hat{\chi}_{\mathrm{BG}}^{-1}(\omega) \approx \sum_{k=0}^{M} (a_k + i b_k)(\omega - \omega_0)^k, \tag{13}$$

where i is the imaginary constant and $\{a_k\}$ and $\{b_k\}$ are sets of real coefficients to be determined. A drive force with N_D frequency components allows for the determination of up to $2N_D$ coefficients, corresponding to two polynomial fits of degree $M = N_D - 1$ of the real and imaginary parts of $\hat{\chi}_{\mathrm{BG}}$. It is possible to perform a low-degree fit with a high number of drives, $M < N_D - 1$, in which case the coefficients are obtained with a least-square optimization method.

While a higher-order fit could in principle describe a more complex $\hat{\chi}_{\mathrm{BG}}$, we find that a linear approximation of each of the two quadratures (four coefficients, requiring two or more drive frequencies) is sufficient to describe the background forces. A higher-order fit is not always numerically stable, and it can introduce artifacts in the compensated data.

Equation (13) is quite general, allowing for a good approximation to any type of linear background force. A special case of Eq. (13) is a polynomial with only two coefficients of the form

$$\hat{\chi}_{\mathrm{BG}}^{-1}(\omega) \approx k(a\omega^2 + ib\omega), \tag{14}$$

where k is the mode stiffness and a and b are fit parameters. In this case it can be shown that the background forces result in an effective cantilever with a renormalized linear-response function $\hat{\chi}'$ of the form of Eq. (2), where the resonance frequency and quality factor are given by

$$\omega_0' = \omega_0 \frac{1}{\sqrt{1 - a\omega_0^2}}, \tag{15}$$

$$Q' = Q \frac{\sqrt{1 - a\omega_0^2}}{1 + bQ\omega_0}. \tag{16}$$

This special case is often assumed when analyzing forces in dynamic AFM [5–7].

V. EXPERIMENTAL RESULTS

We have shown how to mathematically treat the problem of compensating for arbitrary linear background forces, and we proposed a simple method to obtain their response function. We now show an application of this method on soft material surfaces where background forces are typically rather large.

Figure 4 shows dynamic force quadratures [11] on two areas of a polystyrene low-density polyethylene polymer blend (Bruker). F_I is the force in phase with the cantilever motion integrated over one oscillation cycle, representing the conservative forces experienced by the cantilever at different oscillation amplitudes. F_Q is the force quadrature to the cantilever motion integrated over one oscillation cycle, showing the dissipative interaction of the cantilever with its environment and with the surface. The force quadratures represent a direct transformation of the measured data without any model assumptions, providing a physically intuitive way of analyzing the measured cantilever dynamics in terms of conservative and dissipative interactions.

At low amplitudes the uncompensated force quadratures [dashed lines in Figs. 4(b) and 4(c)] show a positive slope in F_I, the signature of a long-range attractive force. The negative slope in F_Q is a signature of a linear damping, in addition to the damping contained in $\hat{\chi}$ which is calibrated far away from the surface. Some hysteresis is also present in both sets of curves, indicating that the background forces are not purely of the type described by the special case of Eq. (14). Notably, the low-amplitude background forces are the same for the two sets of curves, despite being measured over different areas of the sample with very different material properties, confirming that the background forces are not local to the AFM tip.

We use a drive scheme with $N_D = 2$, measured $\hat{d}_{\mathrm{lift}}$ over a polystyrene area of the sample [black circle in Fig. 4(a)], then calculate $\hat{\chi}_{\mathrm{BG}}$ with $M = 1$ in Eq. (13) and apply its compensation to the measured data. The solid lines in

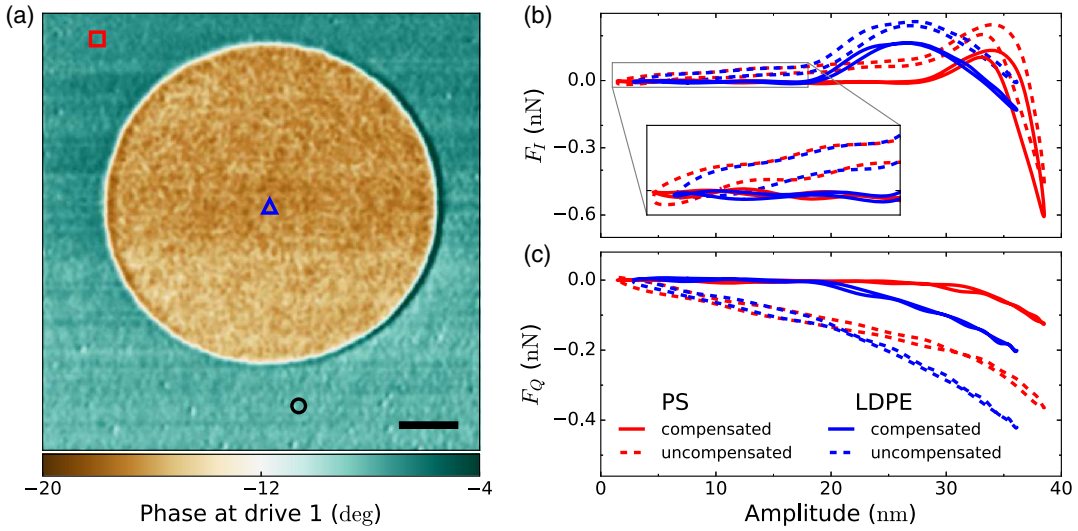

FIG. 4. (a) Phase image at the first drive frequency on a blend of polystyrene (PS) and low-density polyethylene (LDPE). The blue triangle and the red square mark the pixels for which the engaged spectrum is analyzed. The black circle marks the location where the lift motion is measured using the method described in Sec. III. The scale bar is 200 nm. (b),(c) Dynamic force quadratures on PS (red) and on LDPE (blue) at the pixels marked in the corresponding color. Dashed lines show uncompensated measurements and solid lines show compensation for background forces.

Figs. 4(b) and 4(c) show the force quadratures compensated for background forces. The slope at low amplitudes is now missing, as well as most of the hysteretic effects [see inset of Fig. 4(b)]. We note that the compensation calculated over a polystyrene area of the sample has this effect not only for the force quadratures on the polystyrene, but also for those on polyethylene. Taken together, these observations confirm the validity of the assumption that while the background forces change for every pixel of the image, their linear-response function does not change during the whole scan.

Figure 5 shows the same measurement and compensation procedure on a silicone hydrogel sample in a high-humidity environment. The sample presents alternating solid and liquidlike domains [Fig. 5(a)] with very different mechanical response as shown by the peculiar shapes of the

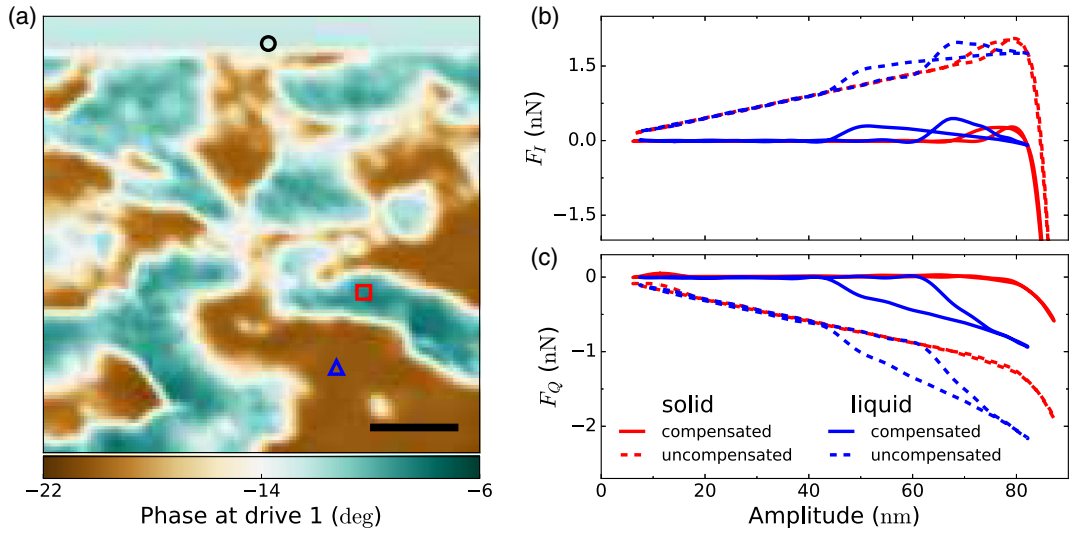

FIG. 5. (a) Phase image at the first drive frequency on a silicone hydrogel (Young's modulus 0.35 MPa) in a high-humidity environment. The blue triangle and the red square mark the pixels for which the engaged spectrum is analyzed. The black circle marks the pixel where the lift motion is measured while scanning. At the top of the image the AFM is left scanning at the lift position, demonstrating that the background forces are independent on the xy position of the tip. The scale bar is 200 nm. (b),(c) Dynamic force quadratures on a solidlike area (red) and on a liquidlike area (blue) at the pixels marked in the corresponding color. Dashed lines show uncompensated measurements and solid lines show compensation for background forces.

force quadratures [Figs. 5(b) and 5(c)]. Also in this sample it is clear how the background-force compensation corrects for the long-range attractive forces and increased dissipation, while at the same time preserving the interesting features of the tip-surface force and the peculiar hysteresis. These will be discussed further in a forthcoming publication.

For the dynamic force quadratures shown, the generic compensation according to Eq. (13) is used. Figure 6 shows a comparison of these curves with the ones obtained from the special, simplified case of Eq. (14). While the simplified case can capture the general slope in the conservative and in the dissipative long-range interactions, it fails to describe the hysteresis in the low-amplitude part of the curves. Thus, the background forces cannot be described by simply redefining the parameters of the cantilever resonance, indicating that a more thorough modeling of the interactions is required.

We show the effect of applying the background-force compensation on the dynamic force quadratures F_I and F_Q. The compensation procedure is, however, general and can be applied to any force reconstruction method. Once the frequency components of the compensated tip-surface force $\hat{F}_{\mathrm{TS}}$ are obtained from Eq. (9), $\hat{F}_{\mathrm{TS}}$ can be fed to any force reconstruction algorithm without further modifications. As an example, in Fig. 7 we calculate the tip-surface force on the polystyrene and on the solid domain of the hydrogel sample with amplitude-dependent force spectroscopy [12] (ADFS), with and without compensation for the background forces. Not compensating for background forces would lead to overestimating the adhesion force by 47% for polystyrene, and by 240% for the solid domain of the hydrogel. The observed peak force would be instead underestimated by about 10% in both cases (not shown in Fig. 7).

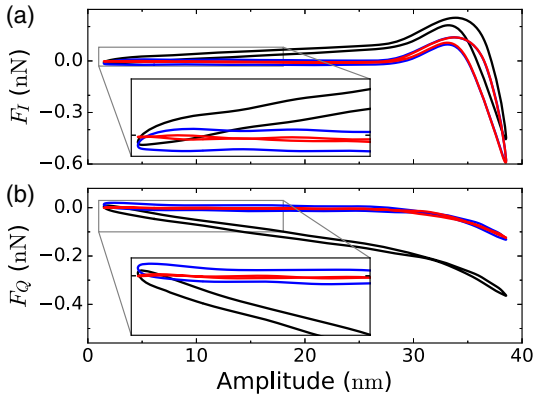

FIG. 6. Comparison of dynamic force quadratures on F_I (a) and F_Q (b) polystyrene: uncompensated curves (black), compensated according to Eq. (13) (red), and according to Eq. (14) (blue). The simplified case of Eq. (14) fails to describe the hysteresis in the low-amplitude region of the curves.

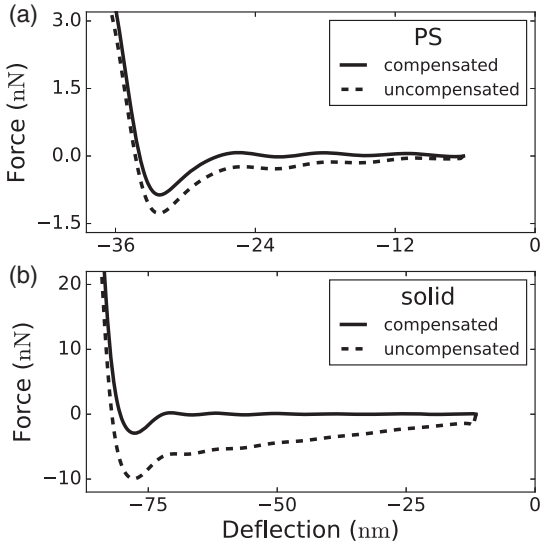

FIG. 7. Tip-surface force on polystyrene (a) and a solid domain of hydrogel (b) reconstructed with amplitude-dependent force spectroscopy [12] (ADFS). The dashed lines show the uncompensated force, and the solid lines the force compensated for background interactions.

VI. SIMULATION OF BACKGROUND FORCES

Because of the nonlinear nature of the tip-surface interaction in dynamic AFM, the dynamics is typically simulated by numerically integrating the differential equation for the cantilever deflection $d(t)$

$$\ddot{d} + \frac{\omega_0}{Q}\dot{d} + \omega_0^2 d = \frac{\omega_0^2}{k}(F_D + F_{\mathrm{TS}} + F_{\mathrm{BG}}). \quad (17)$$

$F_D(t)$ is a known function of time, whereas F_{TS} and F_{BG} are unknown. A variety of models for F_{TS} are available [13] to simulate different types of both conservative and dissipative tip-surface interaction as a function of the cantilever motion $d(t)$ and its velocity $\dot{d}(t)$, and even on the effective position of a moving surface model [14]. On the other hand, no general model for simulating background forces is available, due to the different types of interaction that can give rise to this effect.

In the frequency domain, the background forces can be treated as an effective cantilever linear-response function $\hat{\chi}'$:

$$\hat{F}_{\mathrm{TS}} = \hat{\chi}'^{-1}\hat{d}_{\mathrm{eng}} - \hat{F}_D, \quad (18)$$

where

$$\hat{\chi}'^{-1} = \hat{\chi}^{-1} - \hat{\chi}_{\mathrm{BG}}^{-1}. \quad (19)$$

Transforming $\hat{\chi}'$ into a differential equation is in general very difficult, however, in the special case of Eq. (14) it is possible to simply replace ω_0 and Q in Eq. (17) with ω_0' and Q' as defined by Eqs. (15) and (16):

$$\ddot{d} + \frac{\omega_0'}{Q'}\dot{d} + \omega_0'^2 d = \frac{\omega_0'^2}{k}(F_D + F_{\mathrm{TS}}). \tag{20}$$

Alternatively, it is possible to more generally treat the effect of the background forces on the nonlinear response by introducing an effective drive force $\hat{F}'_D$:

$$\hat{F}_{\mathrm{TS}} = \hat{\chi}^{-1}\hat{d}_{\mathrm{eng}} - \hat{F}'_D, \tag{21}$$

where

$$\hat{F}'_D = \hat{F}_D + \hat{\chi}_{\mathrm{BG}}^{-1}\hat{d}_{\mathrm{eng}}. \tag{22}$$

Once the free, lift, and engaged motions are measured experimentally, Eq. (22) is used to determine the effective drive force $\hat{F}'_D(\omega)$ which is readily transformed to the time domain $F'_D(t)$ via the inverse Fourier transform. The new differential equation

$$\ddot{d} + \frac{\omega_0}{Q}\dot{d} + \omega_0^2 d = \frac{\omega_0^2}{k}(F'_D + F_{\mathrm{TS}}) \tag{23}$$

can now be integrated numerically.

A comparison of the simulated motion d_{sim} using Eqs. (20) or (23), with the measured motion d_{eng}, allows for numerical optimization to find the best-fit parameters of a nonlinear tip-surface force model.

VII. CONCLUSIONS

We derive a mathematical procedure to account for long-range background forces in dynamic AFM, under the assumption of linear interaction and in the limit of a narrow-band measurement. Using intermodulation distortion to detect the onset of tip-surface forces, we accurately measure the background forces at the driven frequencies and extrapolate their linear-response function to undriven frequencies. Applying our procedure to experimental data we demonstrate compensation for background forces on dynamic force quadratures and ADFS force curves, measured on two different soft materials. Given the generality of the compensation procedure and its ease of application to any type of dynamic force reconstruction, our method will be very useful for the determination of material properties with quantitative dynamic AFM.

ACKNOWLEDGMENTS

The authors acknowledge financial support from the Swedish Research Council (VR), the Knut and Alice Wallenberg Foundation, and the Olle Engkvist Byggmästare Foundation. Gunilla Hägg (Star-Lens AB, Åmål, Sweden) is acknowledged for providing the silicone hydrogel sample.

APPENDIX: EXPERIMENTAL AND IMPLEMENTATION DETAILS

All measurements reported were performed in ambient atmosphere at room temperature with commercially available instrumentation.

The measurements on the polystyrene low-density polyethylene blend sample (Figs. 3, 4, and 7) are performed on a Bruker Dimension Icon Atomic Force Microscope. The cantilever used is a MikroMasch HQ:NSC15/AlBS. The fundamental flexural eigenmode of the cantilever and the detector are calibrated with the noninvasive thermal-noise method [9,10], which yields resonance frequency $f_0 = 231.6$ kHz, quality factor $Q = 392.3$, mode stiffness $k = 14.25\ \mathrm{N\,m^{-1}}$, and inverse optical-lever responsivity $\mathrm{invOLR} = 88.63\ \mathrm{nm\,V^{-1}}$. The drive of the acoustic actuation is chosen to have a free oscillation amplitude of 50 nm (100 nm peak to peak) for all the number of drives N_D. The scan in Fig. 4 is performed with a drive composed of two frequencies separated by 500 Hz and centered around the cantilever resonance. The AFM feedback keeps the amplitude at the lower drive frequency constant, at 80% of its free value by adjusting the z extension of the scanner. The scan size is 1.5 μm, the resolution 256×256 pixels, and the pixel time 2 ms, giving a total scan time of less than 5 min.

The measurements on the silicone hydrogel (Figs. 5 and 7) are performed on a JPK NanoWizard3 AFM. The cantilever is a Bruker Tap525. The thermal-noise calibration yields resonance frequency $f_0 = 470.3$ kHz, quality factor Q=626.0, mode stiffness k=86.39Nm^{-1} and inverse optical-lever responsivity $\mathrm{invOLR} = 37.84\ \mathrm{nm\,V^{-1}}$. The amplitude feedback set point is 86% of the free value. The total free amplitude is 105 nm (210 nm peak to peak). The scan size is 1 μm, the resolution 128×128 pixels, and the pixel time 2 ms, giving a total scan time of about 1 min.

For all the measurements reported, a multifrequency lock-in amplifier and dedicated control software (Intermodulation Products AB) are used as an add-on to the AFM hardware and software.

The automatic procedure for measuring the lift oscillation (see Sec. III) works as follows. The scan size of the AFM is set to zero. The z scanner is fully retracted (by setting a very high amplitude set point) and the free intermodulation distortion $\mathrm{IMD_{free}}$ is measured. The original set point is restored to allow the tip to engage the surface again. The set point is repeatedly increased in steps of 0.1% (causing the z scanner to gradually retract) and the IMD is measured for each of the set-point values. To allow the AFM feedback to stabilize and to lower the noise, at each step 100 pixels are acquired (typically requiring 200 ms) and only the last 10 pixels are averaged and included in the calculation of IMD. The procedure continues until the measured IMD decreases to within 3 dB (a factor of 2) of $\mathrm{IMD_{free}}$. The first measurement that satisfies $\mathrm{IMD} < \mathrm{IMD_{free}} + 3$ dB defines the lift oscillation d_{lift} which is then stored. The original scan size and feedback

set point are finally restored and the AFM scan is resumed. The whole procedure requires less than one minute and is fully automated.

When the free and lift response is known, the background-forces linear-response function $\hat{\chi}_{\mathrm{BG}}$ can then be calculated from Eq. (8) at the driven frequencies (2 in the case of Figs. 4 and 5, N_D in Fig. 3). To get $\hat{\chi}_{\mathrm{BG}}$ at all the measured frequencies (32 in the case of Fig. 4, 42 in Fig. 5), a least-square optimization routine (MINPACK) is used to fit Eq. (13) to the measured $\hat{\chi}_{\mathrm{BG}}$.

[1] W.-M. Zhang, G. Meng, J.-B. Zhou, and J.-Y. Chen, Nonlinear dynamics and chaos of microcantilever-based TM-AFMs with squeeze film damping effects, Sensors **9**, 3854 (2009).

[2] C. D. F. Honig, J. E. Sader, P. Mulvaney, and W. A. Ducker, Lubrication forces in air and accommodation coefficient measured by a thermal damping method using an atomic force microscope, Phys. Rev. E **81**, 056305 (2010).

[3] J. E. Sader, R. Borgani, C. T. Gibson, D. B. Haviland, M. J. Higgins, J. I. Kilpatrick, J. Lu, P. Mulvaney, C. J. Shearer, A. D. Slattery, P.-A. Thorén, J. Tran, H. Zhang, H. Zhang, and T. Zheng, A virtual instrument to standardise the calibration of atomic force microscope cantilevers, Rev. Sci. Instrum. **87**, 093711 (2016), Supplemental Material.

[4] B. M. Law and F. Rieutord, Electrostatic forces in atomic force microscopy, Phys. Rev. B **66**, 035402 (2002).

[5] S. Jesse, S. V. Kalinin, R. Proksch, A. P. Baddorf, and B. J. Rodriguez, The band excitation method in scanning probe microscopy for rapid mapping of energy dissipation on the nanoscale, Nanotechnology **18**, 435503 (2007).

[6] J. P. Killgore, D. G. Yablon, A. H. Tsou, A. Gannepalli, P. A. Yuya, J. A. Turner, R. Proksch, and D. C. Hurley, Viscoelastic property mapping with contact resonance force microscopy, Langmuir **27**, 13983 (2011).

[7] R. C. Tung, J. P. Killgore, and D. C. Hurley, Liquid contact resonance atomic force microscopy via experimental reconstruction of the hydrodynamic function, J. Appl. Phys. **115**, 224904 (2014).

[8] D. Platz, E. A. Tholén, D. Pesen, and D. B. Haviland, Intermodulation atomic force microscopy, Appl. Phys. Lett. **92**, 153106 (2008).

[9] J. E. Sader, J. A. Sanelli, B. D. Adamson, J. P. Monty, X. Wei, S. A. Crawford, J. R. Friend, I. Marusic, P. Mulvaney, and E. J. Bieske, Spring constant calibration of atomic force microscope cantilevers of arbitrary shape, Rev. Sci. Instrum. **83**, 103705 (2012).

[10] M. J. Higgins, R. Proksch, J. E. Sader, M. Polcik, S. Mc Endoo, J. P. Cleveland, and S. P. Jarvis, Noninvasive determination of optical lever sensitivity in atomic force microscopy, Rev. Sci. Instrum. **77**, 013701 (2006).

[11] D. Platz, D. Forchheimer, E. A. Tholén, and D. B. Haviland, Interpreting motion and force for narrow-band intermodulation atomic force microscopy, Beilstein J. Nanotechnol. **4**, 45 (2013).

[12] D. Platz, D. Forchheimer, E. A. Tholén, and D. B. Haviland, Interaction imaging with amplitude-dependence force spectroscopy, Nat. Commun. **4**, 1360 (2013).

[13] J. Melcher, D. Kiracofe, S. Hu, S. D. Johnson, S. Balasubramaniam, and A. Raman, VEDA Manual, https://nanohub.org/resources/14934 (2012).

[14] D. B. Haviland, C. A. van Eysden, D. Forchheimer, D. Platz, H. G. Kassa, and P. Leclère, Probing viscoelastic response of soft material surfaces at the nanoscale, Soft Matter **12**, 619 (2016).